Ore Geology Reviews 81 (2017) 296–308

Contents lists available at ScienceDirect

Ore Geology Reviews

journal homepage: www.elsevier.com/locate/oregeorev

Mineralogy, age and genesis of apatite-dolomite ores at the Seligdar apatite deposit (Central Aldan, Russia)

I.R. Prokopyev [a,b,*], A.G. Doroshkevich [a,c], A.V. Ponomarchuk [a], S.A. Sergeev [d]

[a] Sobolev Institute of Geology and Mineralogy Siberian Branch Russian Academy of Sciences, pr. Akademika Koptyuga 3, 630090 Novosibirsk, Russia
[b] Novosibirsk State University, st. Pirogova 2, 630090 Novosibirsk, Russia
[c] Geological Institute Siberian Branch Russian Academy of Sciences, st. Sakhyanova 6a, 670047, Ulan-Ude, Russia
[d] AP Karpinsky Russian Geological Research Institute, pr. Sredny 74, 199106 St. Petersburg, Russia

ARTICLE INFO

Article history:
Received 28 July 2016
Accepted 12 October 2016
Available online 18 October 2016

Keywords:
Dolomite carbonatite
Aldan-Stanovoy shield
Apatite ore
Siberia
Genesis
Age
Mineralogy
Melt and fluid inclusion

ABSTRACT

The Seligdar apatite deposit is located in the Aldan-Stanovoy shield of the Siberian platform in Russia. This deposit is a typical ore deposit of the Nimnyrskaya approximately N-S apatite zone, which is about 400 km long. The genesis of the apatite-dolomite ores at the Seligdar deposit is a matter of debate. This article presents new evidence of the carbonatitic genesis of the apatite-dolomite rocks at the Seligdar deposit based on modern methods of mineralogical, geochronological, melt and fluid inclusion investigations. According to our data, the age of the apatite-dolomite ores is 1880 ± 13 Ma (U-Pb SHRIMP, zircon). Study of melt inclusions indicates that the ores were formed from a carbonate melt of dolomitic composition with alkali (sulphates, chlorides and fluorides of Na and K) and silica components (1–10 wt.%) at a temperature of >1100 °C. The dolomite carbonatites have been subsequently exposed to the intense processes of hydrothermal-metasomatic alteration and metamorphism. The evolution of mineral parageneses from the magmatic apatite-magnetite-dolomite carbonatite stage to the hydrothermal stages with quartz, calcite, monazite-Ce, xenotime-Y, haematite, thorite, thorianite, sulphates and sulphides mineralization agrees with the fluid inclusion regime evolution from the carbonate melt to the chloride brines, and the varying concentrations of the chloride solutions are also described in this article. The investigation of the apatite deposits within the Aldan shield not only allows us to take a new look at the question of their origin but also helps us to study the composition of the ancient mantle, as well as the specifics of apatite-dolomite carbonatite and related hydrothermal Fe and Th-REE mineralization in this region.

1. Introduction

The Seligdar apatite deposit is located in southeastern Russia (Fig. 1). The deposit is situated approximately 30 km southwest from Aldan town in the Central Aldan region of Yakutia (Sakha Republic, East Siberia). The Seligdar deposit is a typical part of the Nimnyrskaya apatite zone (Entin and Tyan, 1984). This zone is confined to the Hardagasky depression and controlled by the ancient Hatystyrsky approximately N-S deep fault. The host rocks of the apatite ore clusters are Archaean metamorphic rocks of the Aldan-Stanovoy shield and terrigenous platform sedimentary rocks. Granitoids and gabbro to plagiogranites from approximately 2000 Ma are spatially associated with the ore clusters.

Age estimates of the apatite-carbonate rocks at the Seligdar deposit range from 2600 to 1400 Ma (Tugarinov et al., 1976; Entin and Tyan, 1984). Dykes of dolerite (1200 Ma) and intrusions of diorite (age unknown) and syenite (Late Mesozoic) are found in the ore clusters of the Nymnyrskaya apatite zone. The complex history of tectonic processes and related magmatism leaves a number of geochronological questions. However, the main question is the origin of the apatite-carbonate ores in this region.

There are several hypotheses of origin for the apatite-carbonate ores of the Seligdar deposit. According to the sedimentary-metamorphic hypothesis, the deposit is confined to the productive carbonate horizon of the Fedorov Archaean suite (Egin and Kichigin, 1973). According to the metasomatic model, there is a potassium-alkaline mafic intrusion at depth, which served as a source of phosphorus for the formation of the hydrothermal-metasomatic apatite ore body (Boyarko, 1983). There is also the hypothesis that the Seligdar ores formed from mantle-crust carbonatites (Smirnov et al., 1976), but because of the lack of association of the apatite-dolomite carbonatites with any ultrabasic alkaline rocks in this region, the hypothesis has not found much support to date.

In this paper, we present new mineralogical, age, melt and fluid inclusion data, which suggest that the Seligdar ores are probably the product of a carbonatite melt.

* Corresponding author at: Sobolev Institute of Geology and Mineralogy Siberian Branch Russian Academy of Sciences, pr. Akademika Koptyuga 3, 630090 Novosibirsk, Russia.
E-mail addresses: prokop@igm.nsc.ru, prokopev_ilya@mail.ru (I.R. Prokopyev).

http://dx.doi.org/10.1016/j.oregeorev.2016.10.012
0169-1368/

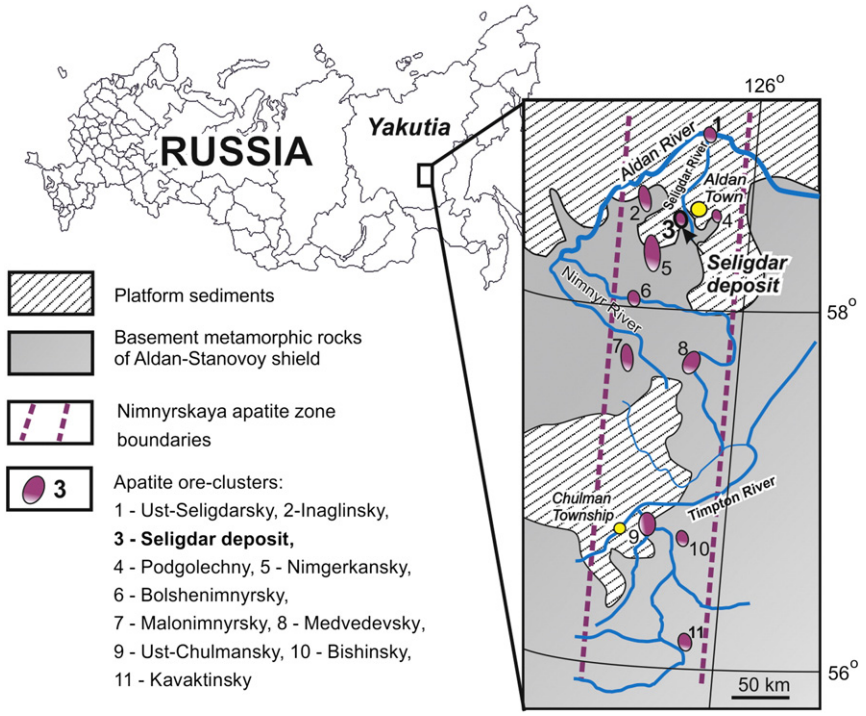

Fig. 1. Position of the Seligdar deposit within the Nimnyrskaya apatite zone in south-east of Russia. (after Entin and Tyan, 1984)

2. Geology

The discovery of the Seligdar apatite deposit occurred during 1972–1982. It was established that the deposit consists of a single round ore body with output parameters of 1.6 × 2.2 km at the surface and estimated total reserves of P_2O_5 of approximately 110–112 Mt (Boyarko, 1983, Fig. 2). The apatite mineralization was traced by drilling as deep as 1660 m. According to the geophysical data, the interpreted depth of the ore body is no less than 3 km. According to morphology, the ore body is a vertically bedded stock-work that is divided into a series of lenses at the periphery. The northern part of the ore body reaches the surface; the southern part is covered by overlying Lower Cambrian carbonate sediments and intrusions of syenite porphyries of Late Mesozoic age (Entin and Tyan, 1984).

The tectonic position of the ore body is determined by the location of the intersecting Tommotsky and Yuhtinsky regional faults trending northeast and northwest, respectively. Faults and cracks within the ore body are filled with brecciated and haematitized apatite-carbonate ores, as well as dykes of trachyte and kersantite. The host rocks in the Seligdar ore field are composed of metamorphosed Archaean deep crystalline rocks, represented by various compositions of gneisses and marbles with minor calc-silicate rocks (Egin and Kichigin, 1973). Gneisses

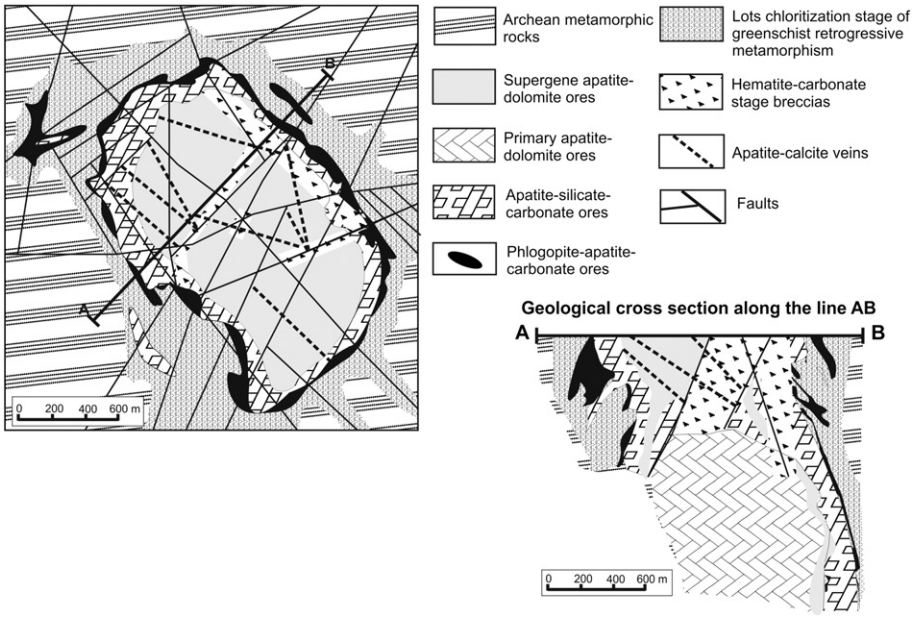

Fig. 2. Schematic geological map and a cross-section through the ore body of the Seligdar deposit. (after Boyarko, 1983)

are represented by biotite, biotite-amphibole, amphibolite, diopside and graphite-containing varieties. The crystalline basement rocks contain bodies of igneous rocks metamorphosed to varying degrees. They are represented by orthoamphibolites of Archaean age and Early Proterozoic quartz-orthoclase-plagioclase rocks. A Late Palaeoproterozoic regional metamorphic event (epidote-amphibolite and amphibolite facies) reworked the rocks of the Central Aldan region (e.g., Gladkochub et al., 2006; Berezkin et al., 2015). Platform deposits consist of terrigenous Vendian sediments, mainly sandstones, limestones, and conglomerates.

According to Boyarko (1983), the Seligdar ore body consists of several concentric zones (Fig. 2). The bulk of the ore body is represented by apatite-dolomite ores located in the central part of the body. The ores are strongly oxidized and subjected to haematitization, sericitization, and chloritization (Boyarko, 1983). The depth of supergene alteration of the apatite-dolomite ores ranges from 50 to 400–600 m (Fig. 2). The apatite-silicate-carbonate zone is located in the peripheral parts of the ore body and bordered by residual outcrop blocks of the surrounding rocks. In the apatite-silicate-carbonate ores, the silicate minerals are mainly phlogopite, talc, actinolite, and secondary quartz. Next, there is a monomineralic phlogopite rim zone with a thickness from a few centimeters to a few meters established along the contact of the apatite-silicate-carbonate ores with the host gneisses. The outermost metasomatic zone is a halo of chloritized greenschist from retrogressive metamorphism, with a thickness of 50 m to 1–2 km.

The modern mineralogical, geochronological, melt and fluid inclusion data, presented in this paper, provide the carbonatite model of the formation of the Seligdar apatite deposit. According to this model the central zone with apatite-carbonate and apatite-silicate-carbonate ores of the Seligdar ore body is a carbonatite and the peripheral zone of the phlogopite rim is probably a fenite (see Discussion).

3. Analytical methods

A representative set of samples for mineralogical, geochronological, melt and fluid inclusion studies of the Seligdar apatite-dolomite ores was collected by the authors during field work in 2015–2016. The rock material is presented by the sample-cores from the exploratory wells of the Seligdar ore field.

The mineral composition of the apatite-dolomite ores of the Seligdar deposit was determined using a scanning electron microscope TESCAN MIRA 3 LMU JSM-6510LV with energy-prefix X-Max Oxford Instruments. To study melt and fluid inclusions in minerals, traditional and modern methods were used. Heating and freezing experiments were carried out using heat chamber TC-1500 design (Osorgin, 1990) with an inert atmosphere of purified argon and a Linkam THMSG-600 stage and include the determination of homogenization temperatures and salt and gas composition of inclusions. Raman spectroscopy was applied to determine the composition of the gas and solid phases in the inclusions (spectrometer JobinYvon LabRAM HR800). Scanning electron microscopy was also used to determine the composition of solid phases in unsealed inclusions.

Concentrations of ore elements and major cations in individual melt inclusions were determined using LA-ICP-MS analysis on a Spectrometer NexION 300D with a laser ablation system NewWave UP 213. Analysis was performed on a wide range of elements: Ca, Mg, Mn, Fe, Sr, Ba, Th, U, Y, Nb, K, Na, Si, Al, Zr, Hf, Ti, and La-Lu. To assess the contents of these elements in the carbonate melt inclusions the NIST 612 glass was used as an external standard. The magnesium content determined by microprobe analysis of uncovered melt inclusions is constant with a range of 13.3–13.5 wt.% (in contrast to calcium and other major dolomite chemical components) and was used as internal standard in calculations. To calculate element concentrations in melt inclusions, an algorithm, based on the formula of Henry Longerich for the calculation of LA-ICP-MS analysis results, was used (Longerich et al., 1996). Element concentrations (wt.% and ppm) were determined by normalizing the absolute results to the ratio of Mg concentration at the interval of inclusion opening to Mg concentration in the inclusion, obtained by microprobe analysis. A similar calculation algorithm is used in many publications dealing with the LA-ICP-MS analysis of fluid inclusions (Günther et al., 1997, 1998; Günther and Heinrich, 1999; Ulrich et al., 2001; Audétat and Pettke, 2003; Heinrich et al., 2003; Borisenko et al., 2011, Prokopyev et al., 2014, 2016, and many other). In order to estimate detection limits depending on the size of the laser beam, analyses were carried out with apertures equal to 15 and 50 μm. For a beam size of 50 μm, detection limits are 0.001 to 1 ppm for all elements (except Si, Ca, Ti, and Cr). With a decrease in aperture from 50 to 15 μm, detection limits are smaller by approximately an order of magnitude.

Mineralogical, melt and fluid inclusion study analyses were carried out at the Analytical Center for multi-elemental and isotope research SB RAS (Novosibirsk, Russia). LA-ICP-MS analyses were performed at the A.P. Vinogradov Institute of Geochemistry SB RAS, Irkutsk, Russia.

Zircon dating using the U-Pb method was carried out on a SHRIMP II at the Center of Isotopic Research, VSEGEI, St. Petersburg, Russia. Zircon crystals were mounted in epoxy along with grains of the TEMORA and 91500 zircon standards. The microanalysis points were selected with the help of optical, BSE, and cathodoluminescence images, which showed the internal structure and zoning of the zircon crystals. The U-Pb ratios were measured using the method recommended by Williams (1998). The intensity of the primary beam of molecular oxygen was 4 nA, and the crater created was 25 μm in diameter and up to 5 μm deep. The data were processed with SQUID software (Ludwig, 2000). The U-Pb ratios were normalized to the value 0.0668 (TEMORA), which corresponds to 416.75 Ma (Black et al., 2003). Individual analyses are within 1σ error, and the calculated concordant ages are within 2σ error. The concordia diagrams were plotted with Isoplot/Ex software (Ludwig, 1999).

The $^{40}Ar/^{39}Ar$ dating was done on monomineralic fractions of phlogopite by stepwise heating (Travin et al., 2009) at the Analytical Center for multi-elemental and isotope research SB RAS (Novosibirsk, Russia). Phlogopite grains were placed into an Al-foil package and stacked in a silica tube. Irradiation was performed in the Cd and B_2C_3-plated channel of the RBT-10/2 reactor (GSC SRIAR, Dmitrovograd, Russia). For calibration we used the international standard biotite (Lp-6) and muscovite (Bern 4 m) (Baksi et al., 1996). The Ar isotope composition was measured on a Noble Gas 5400 mass spectrometer with measurement errors within ±1r. Additional purification of Ar was carried in Zr and Ti-Al SAES getters and in appendix, cooling by liquid nitrogen. The temperature in the reactor was monitored by Al-thermocouple.

4. Geochronology

The available absolute and relative geochronological data (Tugarinov et al., 1976; Entin and Tyan, 1984) for the rocks of Seligdar deposit show wide variations between 2060 and 1400 Ma. Entin and Tyan (1984) proposed two groups of relative dates for the apatite ores of the Seligdar: 1900–1800 and 1500–1400 Ma. Phlogopite (K-Ar dating) from the monomineralic rim zone shows an age of 2060 Ma (Entin and Tyan, 1984). K-Ar methods of dating are susceptible to being reset by secondary processes and must be used carefully for dating of old rocks. Therefore, this date cannot be reliable. U-Pb dating of apatite from apatite-carbonate ores yielded an age of 1855 ± 15 Ma (Tugarinov et al., 1976). Thus, currently available age data for the Seligdar rocks are not sufficient to allow definite conclusions regarding the age of the Seligdar deposit. For this reason, we carried out precise geochronological investigations using the U-Pb SIMS SHRIMP-II method on zircon crystals from the apatite-silicate-carbonate ores (sample Slg-1) and $^{40}Ar/^{39}Ar$ dating of phlogopite from the monomineralic rim zone (sample Sld-69).

Zircon is an accessory mineral of the apatite-silicate-carbonate ores, forming rare crystals up to 0.5 mm in size in apatite-dolomite matrix (Fig. 3c); crystals combine bipyramidal and short prismatic habits (Fig. 3a). The grains have two- or three-phase structures. Some show clear

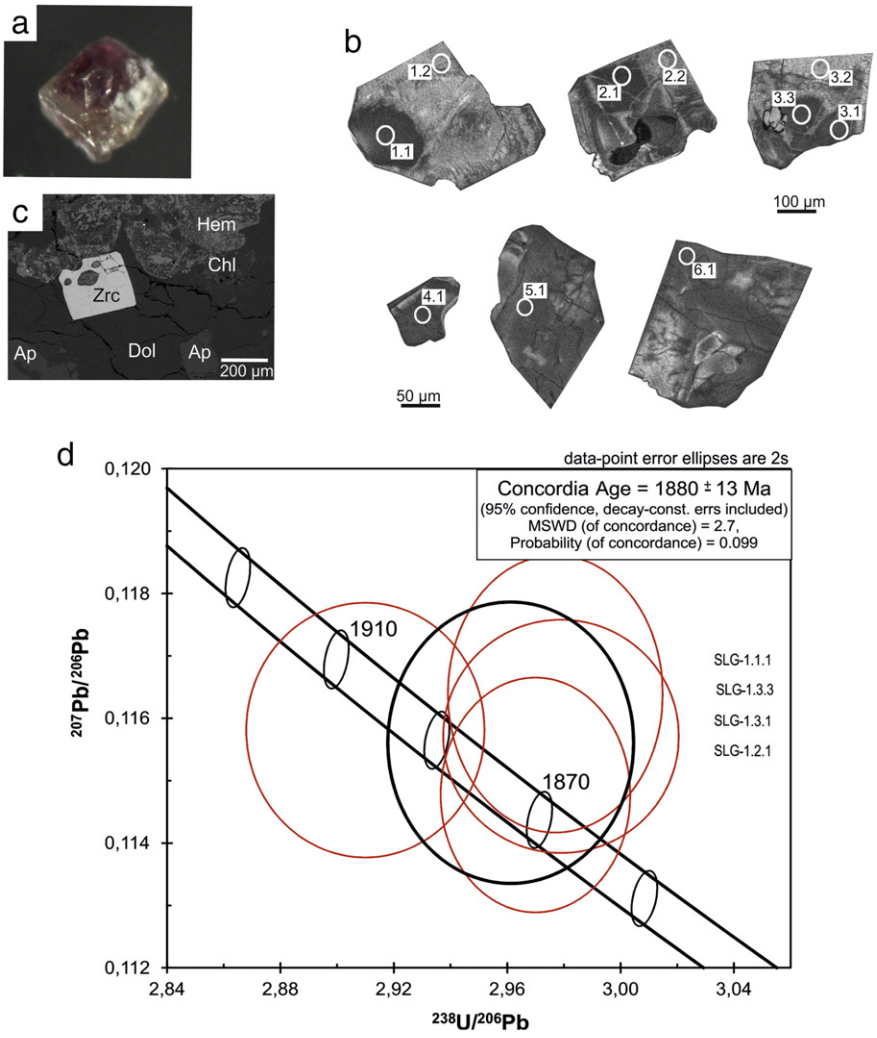

Fig. 3. U-Pb SIMS SHRIMP-II data, sample Slg-1. Zircon photo under the microscope (a), SEM-photo (b), cathodoluminescence images (c), and the U-Pb concordia diagram (d) of zircon grains from the apatite-silicate-carbonate rocks of the Seligdar deposit.

metamict domains with microfractures in cathodoluminescence (CL) images (Fig. 3b). In these domains, the Th/U values vary from 1 to 1.2, and analyses are discordant (Table 1). Some zircons have dark cores with indistinct oscillatory zoning in the rims in a CL image (Fig. 3b). Here, the Th/U values vary from 0.7 to 1.0 (Table 1). The four analyses are concordant and yield an age of 1880 ± 13 Ma (Fig. 3d, Table 1), representing the crystallization age of the Seligdar apatite-silicate-carbonate ores.

$^{40}Ar/^{39}Ar$ age spectra for phlogopite from the monomineralic rim zone consist of 8 steps; temperature was increased from 500 to 1130 °C and produced a stepwise shape: age increases from 250 Ma at low temperatures to 1.8 Ga at high temperatures (Fig. 4, Table 2). It is possible to separate an age plateau of 1761 ± 16 Ma at steps numbers 6, 7 and 8 (Fleck et al., 1977), but taking into account the long-term history, with metamorphic episodes and possible argon loss, we conclude that the last step approaches more closely the real age of formation. In

Table 1
Results of U-Pb SIMS SHRIMP-II analysis of the zircon grains from the apatite-silicate-carbonate rocks of the Seligdar deposit.

Spot	% $^{206}Pb_c$	ppm U	ppm Th	$^{232}Th/^{238}U$	ppm $^{206}Pb^*$	(1) $^{206}Pb/^{238}U$ age		(1) $^{207}Pb/^{206}Pb$ age		% Discordant	(1) $^{238}U/^{206}Pb^*$	±%	(1) $^{207}Pb^*/^{206}Pb^*$	±%	(1) $^{207}Pb^*/^{235}U$	±%	(1) $^{206}Pb^*/^{238}U$	±%	Err corr
SLG-1.4.1	0.94	522	575	1.14	33.3	458	2	1579	40	245	13.564	0.5	0.0976	2.2	0.991	2.2	0.0736	0.5	0.237
SLG-1.5.1	0.68	457	520	1.18	47.8	736	4	1736	28	136	8.261	0.6	0.1062	1.6	1.771	1.6	0.1209	0.6	0.337
SLG-1.6.1	0.67	446	441	1.02	55.9	871	4	1754	26	101	6.902	0.5	0.1073	1.4	2.140	1.5	0.1447	0.5	0.318
SLG-1.2.2	0.92	404	424	1.08	99.4	1607	7	1826	21	14	3.525	0.5	0.1116	1.2	4.358	1.3	0.2832	0.5	0.362
SLG-1.1.2	0.29	395	422	1.10	92.5	1547	7	1847	13	19	3.685	0.5	0.1129	0.7	4.222	0.9	0.2712	0.5	0.546
SLG-1.3.2	0.00	354	331	0.97	93.3	1724	7	1873	10	9	3.263	0.5	0.1146	0.6	4.842	0.7	0.3065	0.5	0.620
SLG-1.2.1	0.17	333	274	0.85	96.6	1870	7	1876	12	0	2.970	0.5	0.1148	0.7	5.325	0.8	0.3365	0.5	0.562
SLG-1.3.1	0.09	274	217	0.82	79.0	1866	9	1891	12	1	2.979	0.6	0.1157	0.7	5.355	0.9	0.3356	0.6	0.652
SLG-1.1.1	0.10	255	181	0.73	75.5	1904	10	1892	13	−1	2.910	0.6	0.1158	0.7	5.486	0.9	0.3436	0.6	0.634
SLG-1.3.3	0.12	270	219	0.84	78.1	1867	8	1902	14	2	2.977	0.5	0.1164	0.8	5.390	0.9	0.3358	0.5	0.552

Notes: errors are 1-sigma; Pb_c and Pb^* indicate the common and radiogenic portions, respectively. Error in standard calibration was 0.29% (not included in above errors but required when comparing data from different mounts). (1) Common Pb corrected using measured ^{204}Pb. The last four analyses are concordant and yield an age of 1880 ± 13 Ma for the zircon from the apatite-silicate-carbonate rocks at the Seligdar deposit.

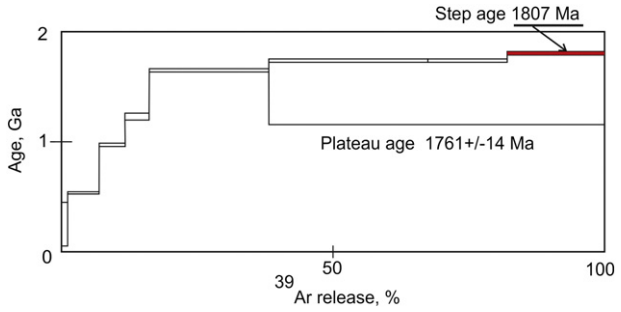

Fig. 4. $^{40}Ar/^{39}Ar$ age spectra for phlogopite from the monomineralic rim zone of the Seligdar ore body.

addition, the K-Ar isotope system in phlogopite is less stable than the U-Pb system in zircon — 350° vs. 800 °C, respectively. Thus, the Ar/Ar data support the obtained U-Pb zircon ages and allow us to infer that the Seligdar rocks are no younger than 1807 Ma.

5. Mineralogy of the apatite-carbonate ores

Boyarko (1983), Bulakh et al. (1984), and Minin et al. (2016) presented detailed studies of the petrography and mineralogy of different types of ores from the Seligdar deposit. Below, we provide a short summary of our investigations of the phase assemblages and mineral compositions in the apatite-dolomite ores of the Seligdar deposit.

The apatite-dolomite ore mineral assemblage is composed of primary ore minerals, ore-related late-stage (hydrothermal) minerals and metamorphic minerals. Dolomite and apatite are the most abundant minerals. In addition to these minerals, magnetite, alkali feldspar, phlogopite and zircon are related to this ore stage. Monazite-(Ce), haematite, calcite, quartz, barite, barite-celestine, anhydrite, thorite, thorianite, xenotime-(Y), siderite, pyrite, and galena are present as late-stage (hydrothermal) minerals. Chlorite, muscovite, epidote, rutile and talc are metamorphic minerals. Representative compositions of the minerals are presented in Tables 3–6.

5.1. Primary ore minerals

Apatite-dolomite ores are massive medium- to coarse-grained rocks composed of highly variable amounts of apatite, magnetite and dolomite, the former varying from in trace amount to essentially monomineralic apatite ores, with an average amount of apatite of 18% (Bulakh et al., 1984).

Apatite forms prismatic crystals of pyramidal habit, sometimes with rounded vertices and edges; crystal size varies from 0.3–1 to 5 cm (Fig. 5a). The mineral colour changes from brown to red depending on haematite impurities. Mineral composition is typical of carbonatites (Hogarth, 1989); it is enriched in Sr, Si and SO_3 (up to 1.6, 1.8 and 1.3, respectively), with average F and Cl contents of 2.9 and 0.5 wt.%, respectively; in individual samples, light REE may range up to 1 wt.% oxide (Table 3). In these cases, there is also approximately 0.4 wt.% Na_2O, indicating the usual coupled REE = Na substitution. The apatite is heterogeneous (Fig. 5b), with varying Si, Sr and REE; microcracks and grain rims have lower amounts of the elements. In these parts, apatite

Table 2
Results of Ar-Ar analysis of the phlogopite from rim zone of the Seligdar deposit.

T, °C	$^{40}Ar/^{39}Ar$	±	$^{38}Ar/^{39}Ar$	±	$^{37}Ar/^{39}Ar$	±	$^{36}Ar/^{39}Ar$	±	^{39}Ar, % cummulative	Age, Ma
500	94.1	9.0	0.09	0.05	0.7	0.4	0.20	0.1	1.1	254.0
625	94.2	0.5	0.06	0.02	0.21	0.09	0.053	0.005	6.9	539.4
725	164.6	1.0	0.01	0.01	0.55	0.12	0.009	0.006	11.7	977.6
825	229.9	4.6	0.04	0.01	0.13	0.08	0.03	0.02	16.1	1232.7
925	340.8	1.8	0.005	0.003	0.02	0.01	0.01	0.005	38.2	1653.9
1000	367.8	1.5	0.010	0.004	0.03	0.01	0.005	0.004	67.4	1742.1
1050	369.2	1.4	0.052	0.006	0.16	0.05	0.013	0.004	82.1	1739.9
1100	388.4	2.0	0.015	0.007	0.007	0.007	0.001	0.005	100.0	1807.5

Table 3
Representative electron-microprobe analyses of apatite, monazite-Ce and mineral of epidote group from Seligdar apatite-dolomite ores, wt.%.

	Apatite					Monazite-Ce in apatite				Monazite-Ce in dolomite				Mineral of epidote group			
SiO_2	0.79	1.75	0.64	0.90	1.05	0.58	0.41	1.90	2.65	0.51	0.58	0.60	0.47	33.61	32.65	33.46	33.2
Al_2O_3	0.00	0.00	0.00	0.00	0.00	0.00	0.00	0.00	0.00	0.00	0.00	0.00	0.00	17.46	15.61	17.29	16.53
FeOt	0.00	0.00	0.00	0.00	0.00	0.00	0.00	0.00	0.00	0.00	0.00	0.00	0.00	11.33	13.21	11.81	11.91
MnO	0.00	0.00	0.00	0.00	0.00	0.00	0.00	0.00	0.00	0.00	0.00	0.00	0.00	0.61		0.71	0.65
MgO	0.00	0.00	0.00	0.00	0.00	0.00	0.00	0.00	0.00	0.00	0.00	0.00	0.00	1.67	1.61	1.67	2.29
CaO	52.72	52.47	53.51	53.41	53.27	2.17	1.44	0.38	0.31	3.12	2.77	2.67	2.24	15.46	14.17	14.65	13.17
Na_2O	0.32	0.28	0.00	0.34	0.28	0.00	0.00	0.00	0.00	0.00	0.00	0.00	0.00	0.00	0.00	0.00	0.00
SrO	1.36	1.37	1.40	1.22	1.35	1.16	0.91	1.37	1.23	1.38	1.31	1.49	1.15	0.00	0.00	0.00	0.00
Ce_2O_3	0.64	0.71	0.00	0.37	0.55	33.84	35.56	32.19	30.63	31.14	31.64	33.84	33.43	8.76	10.69	9.32	11.85
La_2O_3	0.43	0.49	0.00	0.25	0.35	16.04	13.57	22.04	20.99	14.38	14.35	14.21	15.48	4.4	4.91	4.62	3.33
Pr_2O_3	0.00	0.00	0.00	0.00	0.00	2.76	3.55	2.52	1.86	3.58	3.70	3.29	3.66	0.95	1.43	0.84	1.44
Nd_2O_3	0.00	0.00	0.00	0.00	0.37	10.89	12.69	5.60	5.69	11.06	11.58	11.44	12.80	2.67	3.64	3.1	3.41
Sm_2O_3	0.00	0.00	0.00	0.00	0.00	0.83	0.89	0.95	0.78	1.67	1.53	0.92	0.00	0.00	0.77	0.00	0.00
ThO_2	0.00	0.00	0.00	0.00	0.00	1.52	2.91	6.95	9.34	1.19	1.55	1.39	0.00	0.00	0.00	0.00	0.00
P_2O_5	41.75	40.03	42.67	41.36	39.78	28.57	28.16	24.43	24.54	27.69	27.18	28.00	29.12	0.00	0.00	0.00	0.00
SO_3	0.52	0.20	0.32	0.90	1.17	0.81	0.35	0.55	0.32	1.72	1.62	1.37	1.65	0.00	0.00	0.00	0.00
Cl	0.16	1.26	0.23	0.13	0.12	0.00	0.00	0.00	0.00	0.00	0.00	0.00	0.00	0.00	0.00	0.00	0.00
F	2.46	2.99	2.97	3.02	3.10	0.00	0.00	0.00	0.00	0.00	0.00	0.00	0.00	0.00	0.00	0.00	0.00
—F=O_2	1.03	1.25	1.24	1.26	1.30												
Total	99.72	99.81	100.01	100.14	99.59	99.17	100.44	98.88	98.34	97.44	97.81	99.22	100.00	96.92	98.69	97.47	97.78
La/Ce						0.5	0.4	0.7	0.7	0.5	0.5	0.4	0.5	0.5	0.5	0.5	0.3
La/Nd						1.5	1.1	3.9	3.7	1.3	1.2	1.2	1.2	1.6	1.3	1.5	1.0

Note: here and below: FeOt = total iron; 0.00 = below detection limit.

Table 4
Representative electron-microprobe analyses of carbonate minerals from Seligdar apatite-dolomite ores, wt.%.

	Dolomite						Calcite						
SiO_2	0.49	0.30	1.22	0.00	0.00	0.00	0.25	0.19	0.12	0.00	0.00	1.09	0.65
FeOt	0.86	0.67	0.35	0.46	1.36	1.11	0.85	0.27	0.19	0.30	0.24	0.40	0.35
MnO	0.32	0.25	0.00	0.44	0.35	0.81	0.62	0.93	0.67	1.02	0.92	0.72	0.88
MgO	21.11	21.34	21.59	21.29	21.08	20.16	19.45	1.34	1.03	1.23	1.24	1.11	0.23
CaO	29.29	29.12	29.44	29.02	28.64	29.59	30.56	50.68	50.58	50.82	51.45	49.38	49.81
SrO	0.00	0.00	0.00	0.00	0.00	0.00	0.00	0.00	0.00	0.00	0.00	0.00	0.00
Total	52.07	51.68	52.60	51.21	51.43	51.67	51.73	53.41	52.59	53.37	53.85	52.70	51.92

Table 5
Representative electron-microprobe analyses of alkali feldspars from Seligdar apatite-dolomite ores.

Wt.%													
SiO_2	65.53	64.42	65.60	64.34	65.85	65.61	65.09	67.03	66.11	67.72	66.81	69.68	68.05
Al_2O_3	18.48	18.33	18.78	18.27	18.16	18.65	18.67	21.08	21.39	20.62	21.31	19.17	20.44
CaO	0.00	0.00	0.00	0.00	0.00	0.00	0.00	1.68	2.14	1.79	2.13	0.18	1.55
Na_2O	0.44	1.67	1.11	0.44	0.38	0.50	0.77	11.09	10.80	10.50	10.55	11.07	10.68
K_2O	15.62	14.62	14.24	15.74	15.46	15.30	15.46	0.16	0.18	0.13	0.18	0.14	0.08
BaO	0.65	0.70	0.70	0.84	0.94	0.90	0.41	0.00	0.00	0.00	0.00	0.00	0.00
Total	100.72	99.74	100.43	99.63	100.79	100.96	100.40	101.04	100.62	100.76	100.98	100.24	100.80
Formulae based on 8 atoms of oxygen, apfu													
Si	3.006	2.988	3.002	2.997	3.021	3.003	2.993	2.915	2.891	2.943	2.906	3.025	2.954
Al	0.999	1.002	1.013	1.003	0.982	1.006	1.012	1.080	1.103	1.056	1.092	0.981	1.046
Ca	0.000	0.000	0.000	0.000	0.000	0.000	0.000	0.078	0.100	0.083	0.099	0.008	0.072
Na	0.039	0.150	0.098	0.040	0.034	0.044	0.069	0.935	0.916	0.885	0.890	0.932	0.899
K	0.914	0.865	0.831	0.935	0.905	0.893	0.907	0.009	0.010	0.007	0.010	0.008	0.004
Ba	0.012	0.013	0.013	0.015	0.017	0.016	0.007	0.000	0.000	0.000	0.000	0.000	0.000
Mol.% end-members													
Albite (Ab)	4.1	14.6	10.5	4.0	3.6	4.7	7.0	88.8	85.9	87.7	85.7	98.0	89.5
Anorthite (An)	0.0	0.0	0.0	0.0	0.0	0.0	0.0	10.4	13.2	11.6	13.4	1.2	10.1
Orthoclase (Or)	95.0	84.4	88.5	94.7	95.0	94.0	92.4	0.8	0.9	0.7	1.0	0.8	0.4
Celsian	1.0	1.0	1.1	1.2	1.4	1.4	0.6	0.0	0.0	0.0	0.0	0.0	0.0

contains abundant monazite-(Ce) inclusions, with minor thorianite, xenotime-(Y), haematite, quartz and anhydrite (Fig. 5b, c). Sometimes, monazite-(Ce) (Mnz-1), haematite and quartz form microveinlets along microcracks and rims of apatite crystals.

Magnetite forms sub-idiomorphic grains up to 1 cm. This mineral is low in TiO_2 (up to 1.1 wt.%) and usually replaced by haematite. Magnetite contains fine ilmenite (?) lamellae oriented in the [111] direction of the magnetite (Fig. 5d). Rutile and haematite fill the lamellae completely. Minin et al. (2016) assumed that the rutile lamellae are the product of magnetite-rutile solid solution. On the contrary, we propose that rutile and haematite developed within metailmenite (?) lamellae as a result of oxidation.

Dolomite is euhedral and contains FeO_{tot} (up to 2 wt.%) and MnO (up to 0.8 wt.%) (Table 4). This mineral usually contains fine dispersions of monazite-(Ce), haematite, barite and barite-celestine (Fig. 5e). Sometimes, haematite and monazite-(Ce) form a net of microveinlets within the dolomite (Fig. 5f).

Alkali feldspar, phlogopite and zircon are rare minerals. Alkali feldspar is orthoclase (Or_{89-95}) with no anorthite component at all but with small amounts of Na and Ba (Table 5). The mineral shows mesoperthitic textures with albite-oligoclase ($Ab_{87-90}An_{10-13}$) in the core of grains, but almost pure albite occurs intergrown with orthoclase in the rims (Fig. 5g). This observation testifies to an interaction of feldspar grains with late-stage fluid near 500 °C (Parsons and Brown, 1988). Phlogopite occurs as single grains in a dolomite matrix. Concentration of F is below the detection limit; the Fe/(Fe + Mg) value ranges up to 0.28. Phlogopite usually is replaced by chlorite and muscovite.

5.2. Ore-related late-stage (hydrothermal) minerals

The apatite-dolomite ores contain quartz-calcite microveinlets (0.5 cm wide), plus disseminations and areas of hydrothermally altered rocks (Fig. 5h). Anhydrite occurs as single grains in quartz-calcite

Table 6
Representative electron-microprobe analyses of some accessory minerals from Seligdar apatite-dolomite ores, wt.%.

	Xenotime						Thorianite				Thorite		
SiO_2	0.00	0.00	0.00	0.00	0.00	0.00	0.00	0.00	0.00	0.00	17.76	18.26	17.46
FeOt	2.12	2.14	2.30	2.10	1.18	1.98	0.00	0.00	0.00	0.00	0.64	1.66	0.58
MgO	0.00	0.00	0.00	0.00	0.00	0.00	0.00	0.00	0.00	0.00	0.32	0.32	0.35
CaO	0.18	0.00	0.20	0.18	0.00	0.12	0.00	0.00	0.00	0.00	1.62	1.02	1.79
Sm_2O_3	0.45	0.00	0.60	0.80	0.90	0.00	0.00	0.00	0.00	0.00	0.00	0.00	0.00
Gd_2O_3	2.87	2.33	2.20	2.10	1.99	2.75	0.00	0.00	0.00	0.00	0.00	0.00	0.00
Dy_2O_3	6.45	5.07	5.50	5.88	6.12	6.42	0.00	0.00	0.00	0.00	0.00	0.00	0.00
Ho_2O_3	1.19	1.99	0.98	1.29	1.10	0.85	0.00	0.00	0.00	0.00	0.00	0.00	0.00
Er_2O_3	3.24	3.19	3.60	2.89	3.25	3.10	0.00	0.00	0.00	0.00	0.00	0.00	0.00
Yb_2O_3	2.21	2.82	2.60	2.87	2.46	2.70	0.00	0.00	0.00	0.00	0.00	0.00	0.00
ThO_2	0.83	0.72	0.92	1.12	1.15	0.99	90.97	92.29	94.26	92.76	74.35	73.17	74.20
PbO	0.00	0.00	0.00	0.00	0.00	0.00	8.31	6.79	5.78	6.31	0.45	0.73	0.61
Y_2O_3	43.86	43.38	43.58	43.17	43.99	43.42	0.00	0.00	0.00	0.00	2.21	3.12	1.93
P_2O_5	36.69	37.19	36.50	37.20	37.16	36.86	0.00	0.00	0.00	0.00	0.00	0.00	0.00
Total	100.09	98.83	98.98	99.60	99.30	99.19	99.28	99.08	100.04	99.07	97.35	98.28	96.92

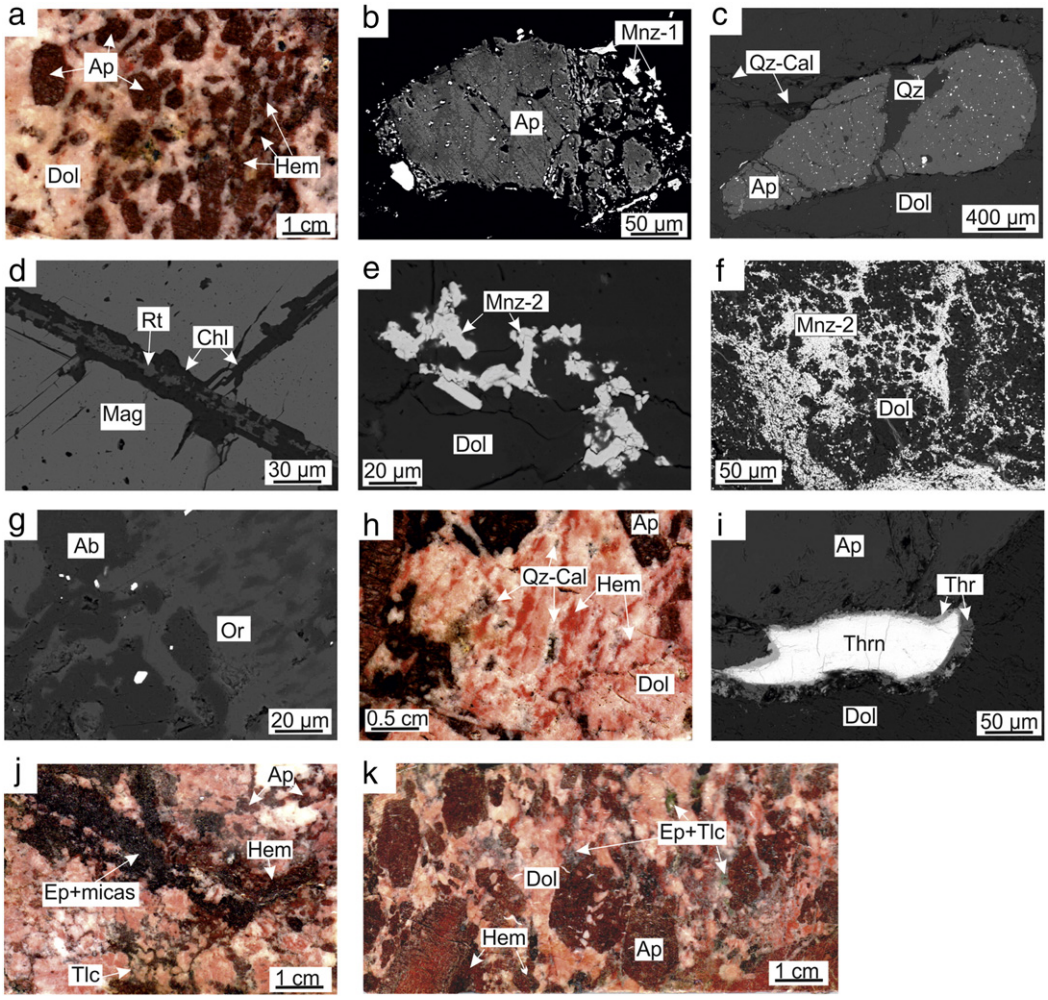

Fig. 5. Photomicrographs (a, h, j, k) and BSE images (b–f, g, i) of mineral assemblages of the apatite-dolomite ores at the Seligdar deposit. (a) Crystals of apatite (Ap) in dolomite (Dol) matrix; (b, c) heterogeneous apatite with monazite-(Ce) (Mnz-1) inclusions and veinlets of quartz (Qz) and calcite (Cal); (d) magnetite (Mag) crystals with ilmenite (?) lamellae which are replaced by rutile (Rut) and chlorite (Chl); (e, f) monazite (Mnz-2) fine dispersions and net of microveinlets in dolomite; (g) orthoclase-albite-oligoclase mesoperthitic texture (Or) with albite (Ab) in the rims of grains; (h); late quartz-calcite (Qz-Cal) and hematite (Hem) veinlets in apatite-dolomite matrix; (i) thorite (Thr) rims around thorianite (Thrn) grains; (j, k) disseminations and patches of metamorphic epidote (Ep), micas, talk (Tlc) in joint zones of apatite-dolomite matrix.

veinlets. Calcite contains FeO (up to 0.4 wt.%), MnO (up to 1 wt.%) and MgO (up to 1.3 wt.%); SrO is below the detection limit (Table 4).

Monazite-(Ce) is present in two generations. The first (Mnz-1) occurs as fine disseminations along microcracks and rims of apatite grains (Fig. 5b, c). It contains ThO_2 (average — 2.4 wt.%), SO_3 (average — 0.45 wt.%), SiO_2 (up to 1.9 wt.%) and CaO (up to 2.7 wt.%) (Table 3). The average La/Ce and La/Nd ratios are 0.6 and 2.5, respectively. The second type (Mnz-2) consists of fine dispersions and sometimes nets of microveinlets in the dolomite (Fig. 5e, f). The concentrations of SiO_2 and CaO in this mineral are similar to those in monazite-Ce from apatite (Table 3), but the ThO_2 content (average — 0.3 wt.%) and the La/Nd ratio (1.5) are lower, and the SO_3 content is higher (average — 1.1 wt.%).

Haematite forms microveinlets within apatite and dolomite grains and replaces magnetite. The last has admixtures of TiO_2 (up to 0.4 wt.%).

Thorianite and xenotime-(Y) both occur as fine mineral inclusions in apatite. Representative compositions of the minerals are presented in Table 6. Commonly, thorite forms rims around thorianite grains (Fig. 5i). PbO concentrations in thorianite reach 8.3 wt.%, whereas thorite contains PbO up to 0.7 wt.% (Table 6).

5.3. Metamorphic minerals

Chlorite and muscovite consist of disseminations and patches in joint zones (Fig. 5k). Minerals of the epidote group, rutile and talc are also present, with talc replacing dolomite and epidote growing over the monazite-Ce along the rims. Sometimes, talc and epidote form monomineralic veinlets in apatite and dolomite (Fig. 5k). Talc contains up to 2 wt.% FeO. Epidote is enriched in light REE; the average La/Ce and La/Nd ratios are 0.4 and 1.5, respectively (Table 3). The ratios are similar to those in monazite-(Ce) from dolomite that indicate an REE inheritance from the latter. Rutile forms as individual grains as well as replaces ilmenite (?) lamellae in magnetite grains. The compositions of both are close to being ideal.

6. Fluid and melt inclusions studies

The first fluid inclusion studies of the apatite-carbonate ores of the Seligdar deposit are described in the earlier works of Puzanov and Partsevsky (1978), Vasilenko et al. (1982), etc. This article for the first time provides data on the presence and composition of melt inclusions in the minerals of the apatite-carbonate ores, as well as the results of studying fluid inclusions of different generations and compositions by using modern investigation methods and analytical equipment (SEM, EPMA, thermo-freezing methods, Raman spectroscopy, and LA-ICP-MS).

6.1. Petrography of inclusions

According to our petrographic investigations of the minerals of the apatite-dolomite ores at the Seligdar deposit, the following types of inclusions are recognized (Fig. 6):

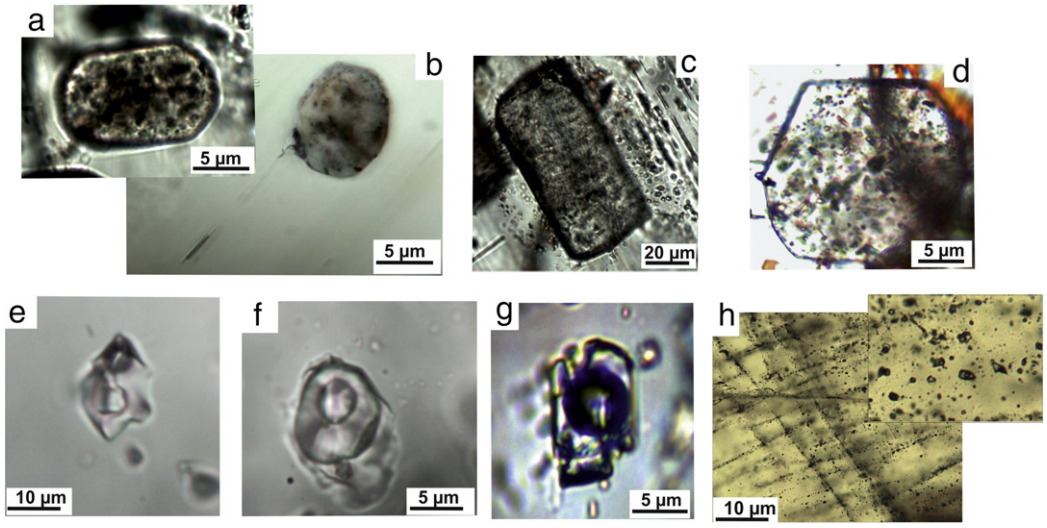

Fig. 6. Inclusions in minerals of the apatite-dolomite ores at the Seligdar deposit. Melt inclusions in apatite crystals: intact melt inclusions (a, b) and opened inclusions (c, d) filled with secondary fluids. Fluid inclusions: primary water-salt (e) and crystal-fluid (f) with liquid CO_2 inclusions in quartz (i- and ii-types); primary gas-liquid inclusion (g) in quartz (iii-type), and secondary gas-liquid inclusions (h) in calcite (iv-type).

1. Melt inclusions: primary silicate-salt-carbonate inclusions in the apatite crystals.
2. Fluid inclusions of different compositions and generations: (i) hydrothermal primary water-salt NaCl/KCl-H_2O with liquid CO_2 inclusions (40 wt.% NaCl-eq.) in quartz crystals and secondary inclusions in apatite; (ii) hydrothermal pseudo-secondary crystal-fluid with CO_2(L) inclusions in quartz, where daughter phases (1–15 vol.% of inclusion) are represented by siderite, and secondary crystal-fluid inclusions with anhydrite crystals in apatite; (iii) primary and secondary crystal-fluid and gas-liquid inclusions of $H_2O \pm$ NaCl-$CO_2(\pm N_2)$ composition with solutions of high (15–30 wt.% NaCl-eq.), medium (5–15 wt.% NaCl-eq.), and low (<1 wt.% NaCl-eq.) salinity in quartz veins, and secondary gaseous fluid inclusions in quartz, calcite, and apatite; and (iv) metamorphic primary and secondary gas-liquid H_2O-CH_4-CO_2 fluid inclusions.

Primary melt inclusions of silicate-salt-carbonate composition were detected in individual prismatic crystals of apatite from the apatite-dolomite ores. The melt inclusions are elliptical- or parallelepiped-shaped and have a negative crystal form vacuoles (Fig. 6a–d). Almost the entire vacuole volume of a melt inclusion is filled with a fine crystalline silicate-salt-carbonate aggregate and fluid phase. The latter occupies 1–3% of the volume of the inclusion. The size of melt inclusions ranges from 5 to 10 to 300 μm. Melt inclusions occur as swarms in the central parts of the apatite crystals and trace the crystal growth zones. Melt inclusions are highly susceptible to secondary hydrothermal-metasomatic processes; they are often opened and filled with secondary fluid inclusions (Fig. 6c, d).

Primary water-salt fluid inclusions (i-type) with cubic crystals of halite or sylvite and a liquid CO_2 fluid phase were discovered in the quartz crystals of the apatite-dolomite ores at the Seligdar deposit (Fig. 6e). The inclusions occur singly or as a swarm in the central parts or crystal growth zones of the matrix crystals. The vacuoles have rounded and rare irregular forms. The average size of inclusions ranges from 10 to 20 μm. Another generation of fluid inclusions (ii) is represented by pseudo-secondary crystal-fluid inclusions with CO_2(L) (Fig. 6f). The pseudo-secondary crystal-fluid inclusions are shaped as vacuoles with close to spherical, elliptical or irregular shapes. The inclusions contain small tabular and irregularly shaped crystals of anhydrite or siderite (1–3 vol.%). The average size of inclusions is 5–20 μm.

Primary and secondary fluid inclusions (iii) in quartz veins of the apatite-dolomite ores have a gaseous $CO_2 \pm N_2$ composition in the fluid phase (Fig. 6g), with cubic crystals of halite present or absent, which produces different salt concentrations in NaCl-eq. The shape of the vacuoles of the primary fluid inclusions is ellipsoidal; they are located in the central part of the matrix crystals or in veins. Healed cracks and cleavage are traced by numerous pseudo-secondary and secondary fluid inclusions, which are widespread in later veins of quartz and calcite. Secondary inclusions have vacuoles of irregular shapes and are characterized by different volume phase ratios. The average size of these fluid inclusions is 5–10 μm. Metamorphic gas-liquid fluid inclusions of different generations (iv) prevail in the minerals of the apatite dolomite ores. They differ by small sizes (1 μm) and CH_4-CO_2 fluid phase composition. Single primary inclusions with rounded vacuole shapes are rare. Numerous secondary fluid inclusions fill the cracks and cleavage planes in the minerals calcite and quartz of the ores.

6.2. Melt inclusion composition and trap conditions

According Raman spectroscopy analyses of intact melt inclusions in apatite crystals, the presence of daughter phases of dolomite (80–99 vol.% of inclusion) and thenardite Na_2SO_4 (approximately 1–3 vol.%) and a CO_2 fluid phase (1–3 vol.%) was established (Fig. 7a, b). SEM-EPMA analyses of opened vacuoles of melt inclusions show the presence of daughter phases of dolomite, silicate and salt composition. The compositions of the silicate phases with K, Na, Ca, Fe, Mg, Al, Si, and O and salt phases with K, Na, Ca, Fe, Cl, F, S, and O were determined only by qualitative analysis because of small crystalline phase sizes. The results of SEM-EPMA and Raman spectroscopy analyses confirm the presence of the silicate and salt components in the composition of the melt inclusions in the apatite-dolomite ores of the Seligdar deposit. The ratios of silicate and carbonate components in different cases vary from 1 to 20 vol.% of the vacuole of the inclusions. The salt component is represented by sulphates (thenardite), chlorides and fluorides of the alkali metals sodium and potassium.

For heating experiments, intact primary melt inclusions of small size (5–15 μm) were used. The results of the heating experiment showed that the fluid phase of the inclusion began to disappear at a temperature above 650 °C, and at a temperature above 700 °C, it was not observed. In the temperature interval from 700 to 800 °C, there was a melting of the daughter phases of the inclusion, and in the interval 1000–1200 °C, approximately 0.8–0.9 of the volume of the crystalline phases in the inclusion vacuole was dissolved. After the heating experiment, during the process of cooling down to room conditions, the daughter crystalline phases crystallized again, which confirms the presence of the salt component in the melt inclusion composition.

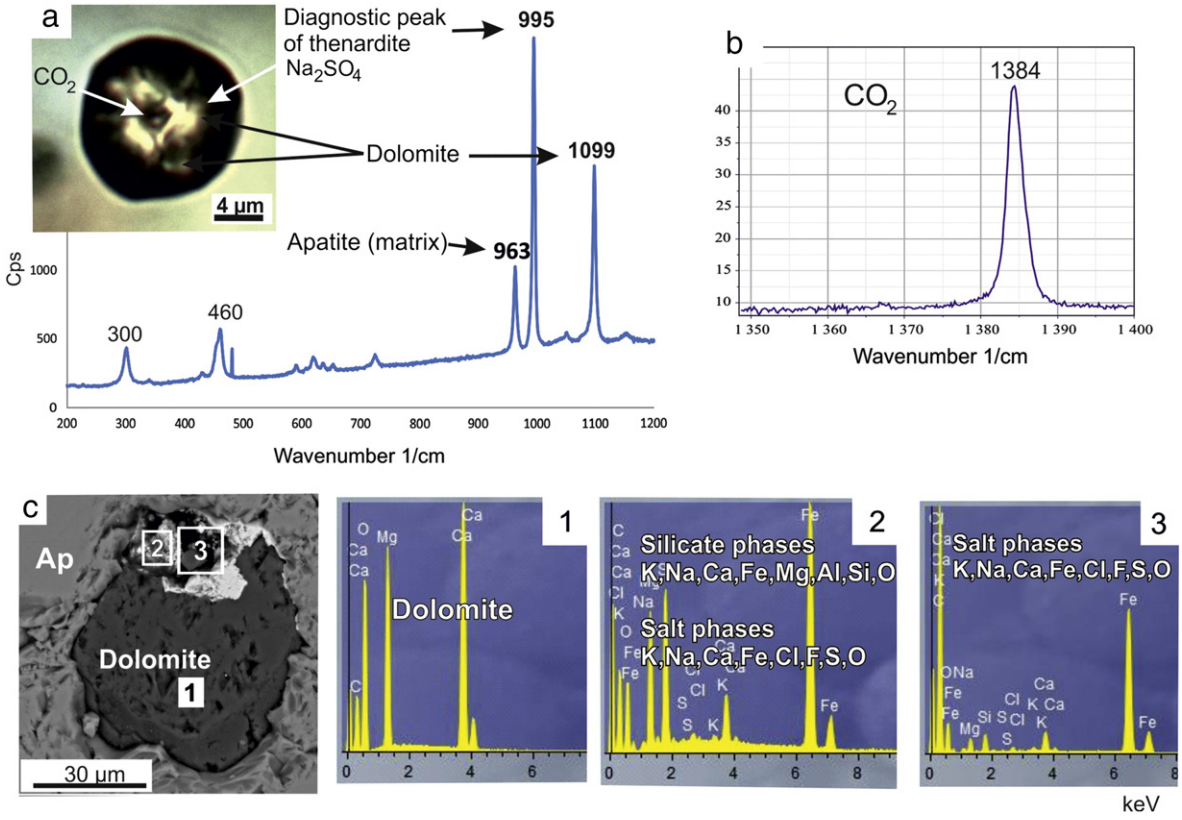

Fig. 7. Results of melt inclusion investigations. Raman spectroscopy data of melt inclusion composition: (a) photomicrograph of inclusion and IR-spectrum of daughter phases — thenardite Na_2SO_4 and dolomite. (b) IR-spectrum of CO_2(L) fluid phase. Determination of the daughter-phases in the opened melt inclusion in apatite according to SEM-EPMA analyses: (c) SEM photo of uncovered melt inclusion with areas of analyses marked by numbers and their corresponding spectra: 1 — dolomite; 2 — silicate (K, Na, Ca, Fe, Mg, Al, Si, O) and salt (K, Na, Ca, Fe, Cl, F, S, O) phases; 3 — salt (K, Na, Ca, Fe, Cl, F, S, O) daughter phases.

6.3. Metals in melt inclusions

The elemental contents and metal-bearing capacity of the melt inclusions were also studied by LA-ICP-MS analysis of the individual inclusions in apatite. The inclusions investigated had representative sizes of 20–40 μm. Approximately 230 melt inclusions were analysed. According to EPMA analyses of uncovered melt inclusions, they have the following concentrations of the main elements (wt.%): Mg — 13.3–13.5, Ca — 21–35, Mn — 0.42–0.3, and Fe — 9–0.15. Because the Mg content determined by microprobe analysis was constant in the range of 13.3–13.5 wt.%, as noted above, it was used as an internal standard for calculations of other metal concentrations in the melt inclusions.

The LA-ICP-MS results show that melt inclusions from the apatite-dolomite ores at the Seligdar deposit contain (ppm): K — 380–5000, Na — 300–700, Sr — 3500–6900, Ba — 700–960, Si — 6900–90,000, Al — 1000–97,000, Ti — 100–1000, La — 1500–200, Ce — 140–160, Nd — 110–150, Th — 100–900, U — 10–50, Y — 220–450, Nb — 7–10, and Yb — 50–70.

6.4. Fluid inclusions study

Primary water-salt fluid inclusions (i-type, Fig. 6e) contain cubic crystals of halite or sylvite, according to SEM data (Fig. 8a), and a liquid CO_2 fluid phase established by Raman spectroscopy. The temperature of homogenization of these fluids ranges from 415 to 465 °C, and the temperature of melting (Tm) of halite crystals is 300–380 °C, which corresponds to a concentration of 38–42 wt.% NaCl-eq. Homogenization of CO_2 to the liquid phase in the water-salt fluid inclusions occurs at +10 to +12 °C, which corresponds to its density of 0.847–0.860 g/cm^3 and a minimum estimated trapping pressure of 220–270 MPa.

According to SEM and Raman spectroscopy data, pseudo-secondary crystal-fluid inclusions (ii-type, Fig. 6f) contain crystalline phases of anhydrite or siderite and a CO_2(L) fluid phase (Fig. 8b, c). These two groups of fluid inclusions that differ by crystalline composition are classified as a single type because of their close location within the same mineral matrix, as well as their similar homogenization temperature interval of 315–385 °C.

Primary and secondary crystal-fluid and gas-liquid inclusions (iii-type) have a $H_2O \pm NaCl$-$CO_2(\pm N_2)$ composition. Crystal-fluid inclusions contain cubic crystals of halite and a CO_2-containing gaseous fluid phase. Homogenization of crystal-fluid inclusions occurs at 250–300 °C. The salt concentrations range from 15 to 30 wt.% NaCl-eq. Secondary two-phase (gas-liquid) fluid inclusions have salt concentrations of 1–15 wt.% NaCl-eq. and homogenize at temperatures of 150–250 °C. They differ in the variation of the CO_2-N_2 (N_2 — 1–9.5 vol.%) fluid phase composition (Fig. 8d). The homogenization temperature of gas-dominated fluid inclusions is approximately 100–150 °C, and salinity is <1 wt.% NaCl-eq. Metamorphic, predominantly secondary, gas-liquid fluid inclusions (iv-type) of the H_2O-CH_4-CO_2 composition have an interval of homogenization temperatures of 300–100 °C.

7. Discussion

7.1. Genesis of the apatite-dolomite ores

Boyarko (1983) interpreted the formation of the apatite-silicate-carbonate ores as a result of the interaction of phosphorous fluids from a buried mafic intrusion at depth and enclosing carbonate rocks.

In our opinion, this model has a number of serious discrepancies with geological reality. First, it is difficult to imagine an intrusion of mafic composition so high in phosphorus that it forms the enormous apatite-rich zones, and there are no credible mafic bodies with abnormally high contents of phosphorus within the ore clusters of the Nimnyrskaya apatite zone. Second and importantly, not all apatite-carbonate clusters contain carbonate sediments (Fyodorovskaya suite)

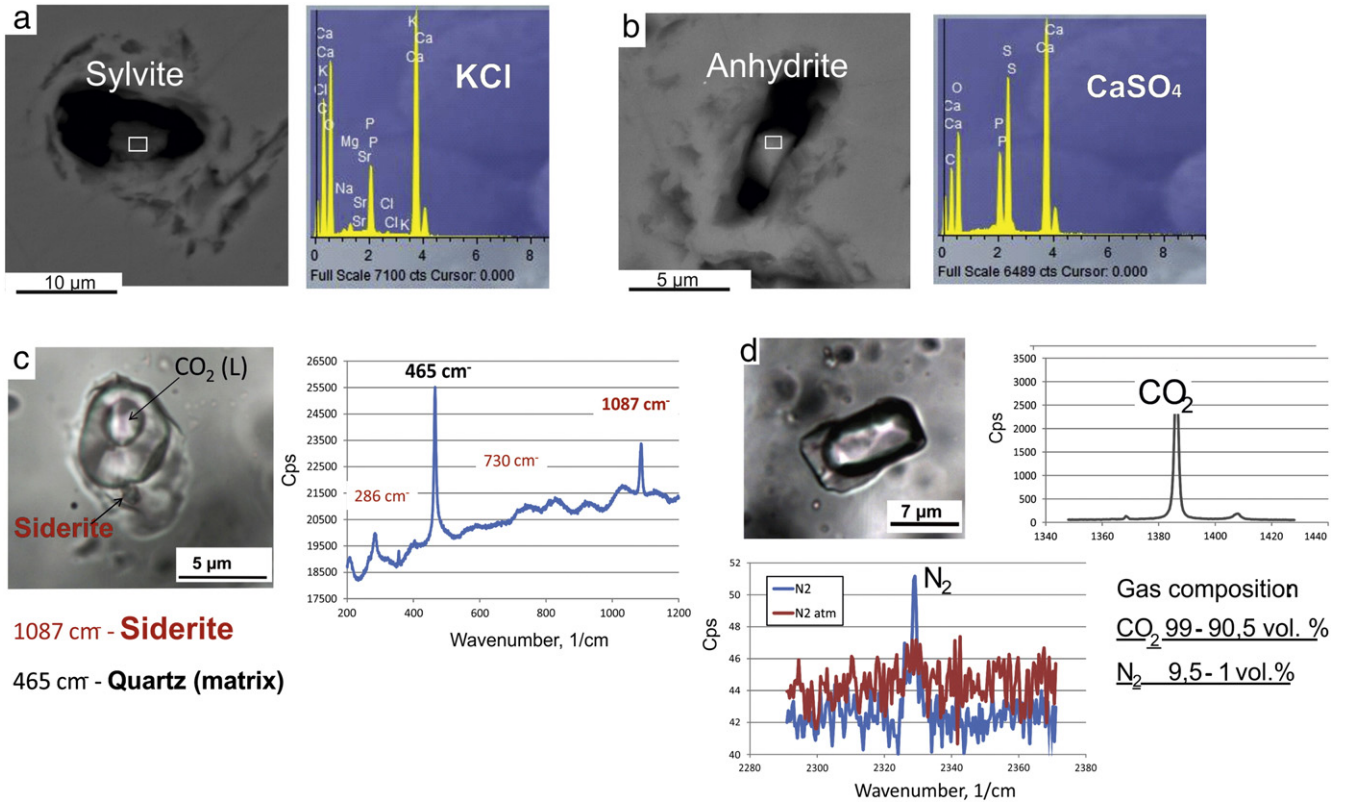

Fig. 8. Results of fluid inclusion investigation. Composition of water-salt fluid inclusion (i-type) by SEM data (a). Determination of daughter phases and fluid phase of the crystal-fluid inclusion (ii-type) by SEM and Raman spectroscopy data (b, c). Gas composition of the fluid phase of the gas-liquid inclusion (iii-type) according to Raman investigations (d).

required for the formation of the apatite-carbonate metasomatic rocks, as geologically mapped (Egin and Kichigin, 1973). According to Berezkin et al. (2015), the concentration of P_2O_5 in the Fyodorovskaya suite does not exceed 0.04 wt.%. The phlogopite monomineralic zone located at the contact of the apatite-dolomite massif with country rocks is most probably fenite. This rock is typically associated with carbonatites (e.g., Le Bas, 2008; Pirajno et al., 2014). Currently detailed mineralogical, geochronological, melt and fluid inclusion data demonstrate a definite answer regarding the model of the formation of the Seligdar apatite deposit.

A schematic summary of the proposed multi-stage model for the formation of the apatite-dolomite ores at the Seligdar deposit is shown in Fig. 10. Melt inclusions investigations (SEM, microprobe, and Raman analyses) show that the apatite-dolomite ores of the Seligdar deposit were formed from a fluid-rich carbonate melt of dolomitic composition with minor silica and alkali contents at a temperature > 1000 °C (according thermometric data). It is usually assumed that dolomite carbonatites are generated as primary mantle melts or that they are the products of calcite magma differentiation. The second scenario does not seem to apply to the Seligdar rocks because there are no geological and mineralogical data on the presence of early calcite carbonatites within the Seligdar ore field. Primary dolomite melts do not usually have associated alkaline silicate rocks (e.g., Bailey, 1989; Vrublevskii et al., 2003; Bell and Rukhlov, 2004; Chakhmouradian et al., 2009; Doroshkevich et al., 2007a, 2007b, 2010; Bailey and Kearns, 2011) or the latter are present in only a limited volume (e.g., Harmer and Gittins, 1998; Harmer, 1999; Agashev et al., 2008). The Seligdar deposit certainly fulfills this criterion because there are no associated intrusive or extrusive alkaline silicate rocks, excluding associated fenites (monomineralic phlogopite rim zone).

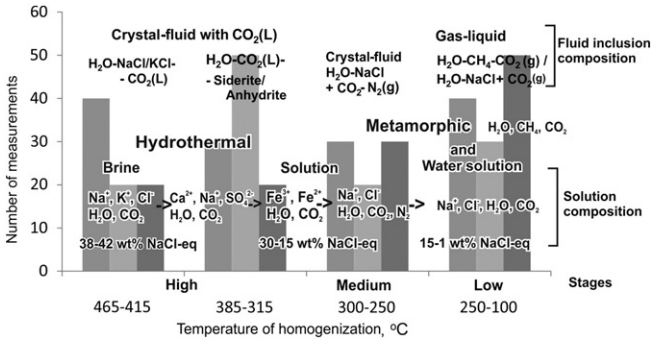

Fig. 9. Scheme of composition and evolution of hydrothermal solution at the Seligdar deposit according to fluid inclusion data.

Experimental studies confirm that primary dolomite melts contain varying amounts of alkalis (0.2 to 7 wt.%) and other components, such as silica (1 to 11 wt.%) (e.g., Otto and Wyllie, 1993; Dalton and Wood, 1993; Sweeney, 1994; Klemme et al., 1995; Sweeney et al., 1995; Dalton and Presnall, 1998; Lee and Wyllie, 1998; Foley et al., 2009). The concentration of silica and alkalis and the K/Na ratio depend on the equilibrium mineral assemblage (e.g., presence and quantity of amphibole and phlogopite in a source) (e.g., Sweeney et al., 1995; Dalton and Wood, 1993; Klemme et al., 1995). On the other hand, the amount of alkalis in primary dolomite carbonatites ranges up to 1 wt.%, and the concentration of silica varies from a fraction to 10 wt.%. Meanwhile, the carbonatites typically are surrounded by fenites or phlogopite zones that testify to the primary magma enrichments in these elements. In the Seligdar apatite-dolomite ores, the alkalis and silica mostly reside in alkali feldspar and phlogopite, and the contacts with country rocks are marked by phlogopite zones. In addition, these components are defined in melt inclusions (alkali salt sulphates, chlorides and fluorides of Na and K, and silicates of K, Na, Ca, Fe, Mg, Al, Si, and O composition), although their concentrations in melts are unlikely to have been high. In contrast, the Seligdar dolomite melt was enriched in SO_3. The activity of this element can be observed from early to late stages of emplacement and is indicated by the enrichment of SO_3 in early apatite and late monazite-Ce and by the presence of sulphates in melt and fluid inclusions and in the rocks.

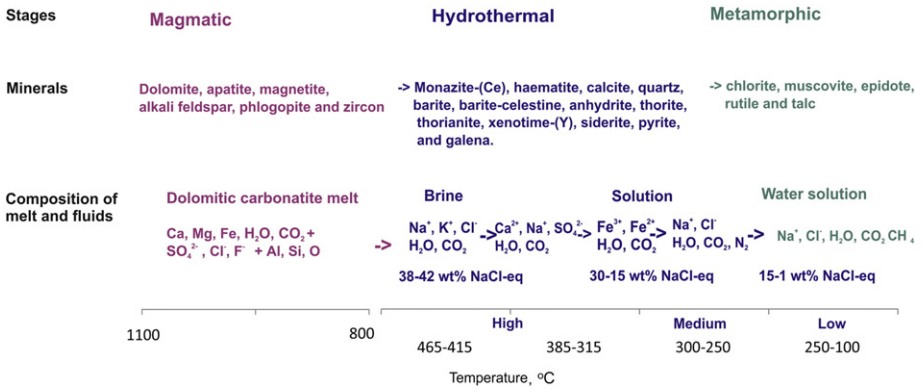

Fig. 10. Evolution of mineral composition and PTX-parameters of formation of the apatite-dolomite ores at the Seligdar carbonatite deposit.

The dolomite carbonatites have been exposed to the intense processes of hydrothermal-metasomatic alteration and metamorphism, which are reflected in the evolution of mineral parageneses and fluid inclusion composition. Study of fluid inclusions showed that the hydrothermal processes took place through high-, medium- and low-temperature hydrothermal stages (Fig. 9). According to the highly concentrated water-salt inclusions and the crystal-fluid with liquid CO_2 inclusions, the dolomitic melt evolved to the chloride brine-solution with an H_2O-NaCl-CO_2(L) composition and a concentration of 38–42 wt.% NaCl-eq. at T > 415–465 °C and pressure 220–270 MPa. These brines are likely responsible for the removal of REE and Th from apatite to form the Th-rich monazite-(Ce), xenotime-(Y) and thorianite grains. Experimental studies demonstrate that REE minerals generally nucleate as a product of fluid-induced REE redistribution within apatite (e.g., Harlov et al., 2002, 2005; Harlov and Förster, 2003). Fluids involved in REE transport and deposition have a high activity of ligands (F, Cl, CO_2(L), SO_4) and brines (e.g., NaCl) (e.g., Williams-Jones et al., 2012; Tropper et al., 2011, 2013). Data on Th solubility is limited, but the experiments show that fluids responsible for Th remobilization are commonly rich in acid anions (Cl, F, SO_4) (e.g., Altmaier et al., 2004; Hetherington and Harlov, 2008). These experimental studies support our fluid inclusion and mineralogical observations that fluids with high concentrations of chlorides promote the internal redistribution of REE and Th within apatite.

The evolution of fluids at decreasing temperatures (385–315 °C) produces a decrease of chloride concentration in solutions, and the salt composition changes to a calcium-sulphate (Ca^{2+}, Na^{+}, SO_4^{2-}, H_2O, and CO_2) solution composition and then further to an oxidized carbonate-ferrous (Fe^{3+}, Fe^{2+}, H_2O, and CO_2) solution composition. The fluids are responsible for the formation of the late quartz-calcite veinlets with sulphates, monazite-Ce and haematite mineralization. The mineral association and compositions of minerals (e.g., high SO_3 in monazite-Ce) confirm the calcium-sulphate composition and high oxidation state of the metasomatic fluids. The changes in the fluid composition provide the different styles of REE mineralization (monazite-(Ce) has lower Th and La/Nd ratio compared to monazite-(Ce) from apatite). According to Li and Zhou (2015), the multiple stages of hydrothermal REE remobilization take place at a high activity as anionic ligands, as well as Ca and Na.

In the medium-temperature stage at 300–250 °C, the salinity drops to 30–15 wt.% NaCl-eq., and the fluid phase differs sharply by composition variations in CO_2-N_2(gas), which points to variations of the acid-reducing balance. At the late low-temperature stage, the salinity of the hydrothermal solution decreases from 15 to 1 wt.% NaCl-eq., and the temperature drops from 250 to 150 °C. Medium-low concentrations of chlorine hydrothermal solutions are responsible for the formation of hydrothermal quartz veinlets with rare pyrite and chalcopyrite grains.

Regional metamorphism of the epidote-amphibolite facies produced talc-epidote-chlorite assemblages in the Seligdar carbonatites. The indicators of these processes too are gas-liquid inclusions with methane and carbon dioxide formed by decarbonation. The homogenization temperatures of these inclusions confirm the action of metamorphism at low temperatures, with the temperatures decreasing from 300 to 100 °C.

7.2. Age of intrusion and geodynamic implications

Emplacement of the Seligdar rocks was coeval with Late Paleoproterozoic (1.88–1.85 Ga) post-collisional processes within the Siberian craton. In this period, post-collision extension followed compression by the collision of several Archaean and Early Paleoproterozoic blocks, which formed the Siberian craton (e.g., Gladkochub et al., 2006, 2012). Mafic dyke swarms in the Aldan and Irkutsk promontory regions, and basalts from the volcanoplutonic belt in the Baikal uplift were formed during this time interval, 1.86–1.87 and 1.84 Ga, respectively (Ernst et al., 2016; Shokhonova et al., 2010). Recent geochronological studies have revealed the ages of layered ultramafic-mafic massifs close to 1.86–1.88 Ga in the south of Siberia (Popov et al., 2009; Tolstykh et al., 2008; Mekhonoshin et al., 2016). In addition, numerous granitic massifs and felsic volcanic rocks were generated within the Siberian craton (e.g., Donskaya et al., 2005; Larin et al., 2000; Neimark et al., 1998; Nozhkin et al., 2003; Turkina et al., 2003). The age of formation of the Seligdar carbonatites demonstrates the link between carbonatites and major LIP in Siberia (Ernst et al., 2016; Ernst and Bell, 2010).

Temporary association of mafic rocks, carbonatites and granites during post-collision extension testify that mantle melts were important agents in the reworking of crustal material. The radiogenic isotope data for the basalts of the Baikal uplift suggest such an association (Shokhonova et al., 2010). Moreover, local zones of extension and higher permeability of the crust might have facilitated the rapid ascent of the carbonatitic magmas to the surface. For example, this process has been described for the Himalayan carbonatites in China (Hou et al., 2006) and for potassic and ultrapotassic rocks in the Northern Tibetan Plateau (Guo et al., 2005). We infer that the formation of the Seligdar rocks was related to the processes discussed above.

Unfortunately we could not determine the age of the hydrothermal mineralization stage. We think that the hydrothermal stage occurred during the process of cooling and differentiation of the primary carbonatite magma (i.e. at 1880 Ma) and not during subsequent metamorphic events. It could be indicated by the temperature and composition of the orthomagmatic fluids. The metamorphism of the amphibolite facies in this region took place a little later, estimated at about 1.83 billion years (Berezkin et al., 2015), which was much later replaced by a low-temperature phases of retrograde metamorphism.

8. Conclusions

1. Melt inclusions investigations demonstrate that apatite-dolomite ores of the Seligdar deposit were formed from a fluid-rich carbonatite melt of dolomitic composition with the presence of alkali

(sulphates, chlorides and fluorides of Na and K) and silica (silicates of K, Na, Ca, Fe, Mg, Al, Si, and O) components at temperatures of > 1100 °C.

2. In geological terms, the Seligdar intrusion is a concentrically zoned carbonatite body with an apatite-silicate-dolomite composition in the centre and a rim of monomineralic phlogopite fenitization zones at the contact. According U-Pb SHRIMP data (zircon), the age of the dolomite carbonatites is 1880 ± 13 Ma, which is consistent with the Ar/Ar data (on phlogopite) showing the minimum age of the phlogopite zone at 1807 Ma.

3. The apatite-dolomite ores were affected by intense processes of hydrothermal-metasomatic alteration and metamorphism. Mineralogical and fluid inclusion investigations showed the evolution of mineral parageneses and fluid inclusion composition.

   (i) At first, the dolomitic melt evolved to a chloride brine-solution of 38–42 wt.% NaCl-eq. concentration at T > 415–465 °C and pressure 220–270 MPa. These brines were responsible for the removal of REE and Th from apatite to form the Th-rich monazite-(Ce), xenotime-(Y) and thorianite.
   (ii) Then, the salt composition changed to a calcium-sulphate (Ca^{2+}, Na^{+}, SO_4^{2-}, H_2O, and CO_2) solution composition and further to an oxidized carbonate-ferrous (Fe^{3+}, Fe^{2+}, H_2O, CO_2) solution composition at temperatures of approximately 385–315 °C. At this stage, the late quartz-calcite veins with sulphates, monazite-Ce and haematite mineralization were formed.
   (iii) The next hydrothermal stages from medium (300–250 °C) to low (250–150 °C) temperatures had H_2O-NaCl-CO_2-N_2(gas) composition, with decreasing salinity from 30 to 15 to 1 wt.% NaCl-eq. Dropping temperatures were responsible for the formation of hydrothermal quartz veinlets with rare pyrite and chalcopyrite grains.
   (iv) The metamorphic fluids of gas-liquid inclusions with methane and carbon dioxide (formed by decarbonation) indicated regional metamorphism of the epidote-amphibolite facies, with temperatures decreasing from 300 to 100 °C. The talc-epidote-chlorite assemblages were formed at these stages.

Future research

The Nimnyrskaya apatite ore zone, measuring approximately 400 km in length, within the Aldan-Stanovoy shield of the Siberian platform in Russia contains more than ten deposits of the Seligdar type (Fig. 1). These deposits are poorly studied in terms of their genesis, mineralogy, geochronology and geochemistry. Our investigation of the apatite-dolomite carbonatites at the Seligdar deposit has shown the importance and relevance for future studies of the apatite deposits in the Aldan shield, which are opening a window for understanding the ancient mantle composition, as well as understanding of the specific magmatic, hydrothermal, and metamorphic processes and related apatite, Fe and Th-REE ore mineralization in this region.

Acknowledgements

This work is supported by the Russian Science Foundation (RSF), grant # 15-17-20036. The authors gratefully thank Prof. Franco Pirajno for editorial comments, and Dr. Richard Ernst and an anonymous reviewer for the reviews, which led to significant improvement of the manuscript.

References

Agashev, A.M., Pokhilenko, N.P., Takazawa, E., McDonald, J.A., Vavilov, M.A., 2008. Primary melting sequence of a deep (>250 km) lithospheric mantle as recorded in the geochemistry of kimberlite–carbonatite assemblages, Snap Lake dyke system, Canada. Chem. Geol. 255 (3), 317–328.
Altmaier, M., Neck, V., Fanghanel, T., 2004. Solubility and colloid formation of Th(IV) in concentrated NaCl and $MgCl_2$ solution. Radiochim. Acta 92, 537–543.
Audétat, A., Pettke, T., 2003. The magmatic-hydrothermal evolution of two barren granites: a melt and fluid inclusion study of the Rito del Medio and Canada Pinabete plutons in northern New Mexico (USA). Geochim. Cosmochim. Acta 67, 97–121.
Bailey, D.K., 1989. Carbonate melt from the mantle in the volcanoes of South East Zambia. Nature 388, 415–418.
Bailey, D.K., Kearns, S., 2011. Dolomitic volcanism in Zambia: Cr and K signatures and comparisons with other dolomitic melts from the mantle. Volcanism and Evolution of the African Lithosphere, pp. 211–222, http://dx.doi.org/10.1130/9780813724782 (Boulder, Colorado, GSA Special Papers 478, ISBN: 978-0-8137-2478-2).
Baksi, A.K., Archibald, D.A., Farrar, E., 1996. Intercalibration of $^{40}Ar/^{39}Ar$ dating standards. Chem. Geol. 129, 307–324.
Bell, K., Rukhlov, A.S., 2004. Carbonatites from the Kola Alkaline Province: origin, evolution and source characteristics. Phoscorites and Carbonatites from Mantle to Mine: The Key Example of the Kola Alkaline Province. Mineral. Soc. Series Vol. 10, pp. 433–468.
Berezkin, V.I., Smelov, A.P., Zedgenizov, A.N., Kravchenko, A.A., Popov, N.V., Timofeev, V.F., Toropova, L.I., 2015. The Geological Structure of the Central Part of the Aldan-Stanovoy Shield and Chemical Compositions of the Early Precambrian Rocks (South Yakutia), Novosibirsk. p. 459 (in Russian).
Black, L.P., Kamo, S.L., Allen, C.M., 2003. TEMORA 1: a new zircon standard for Phanerozoic U–Pb geochronology. Chem. Geol. 200, 155–170.
Borisenko, A.S., Borovikov, A.A., Vasyukova, E.A., Pavlova, G.G., Ragozin, A.L., Prokopyev, I.R., Vladykin, N.V., 2011. Oxidized magmatogene fluids: metal-bearing capacity and role in ore formation. Russ. Geol. Geophys. 52, 144–164.
Boyarko, G.Y., 1983. Geological and Geochemical Features of the Seligdar Apatite Deposits (PhD thesis, Tomsk, 121 pp. (in Russian)).
Bulakh, A.G., Zolotarev, A.A., Bobrova, I.P., Gulii, V.I., Vande-Kirkov, Y.V., 1984. The main features of mineralogy and genesis of the Seligdar apatite deposit (Aldan crystalline shield). Zapiski vsesoyuznogo mineralogicheskogo obchestva Vol. CXIII (4), pp. 398–410 (in Russian).
Chakhmouradian, A.R., Böhm, C.O., Demèny, A., Reguir, E.P., Hegner, E., Creaser, R.A., Halden, N.M., Yang, P., 2009. "Kimberlite" from Wekusko Lake, Manitoba: actually a diamond-indicator-bearing dolomite carbonatite. Lithos 112S, 347–357.
Dalton, J.A., Presnall, D.C., 1998. The continuum of primary carbonatitic–kimberlitic melt compositions in equilibrium with lherzolite: data from system CaO-MgO-Al_2O_3-SiO_2-CO_2 at 6 GPa. J. Petrol. 39, 1953–1964.
Dalton, J.A., Wood, B.J., 1993. The compositions of primary carbonate melts and their evolution through wallrock reaction in the mantle. Earth Planet. Sci. Lett. 119, 511–525.
Donskaya, T.V., Gladkochub, D.P., Kovach, V.P., Mazukabzov, A.M., 2005. Petrogenesis of Early Proterozoic postcollisional granitoids in the southern Siberian craton. Petrology 13 (3), 253–279.
Doroshkevich, A.G., Ripp, G.S., Viladkar, S., 2010. Newania carbonatites, Western India: example of mantle derived magnesium carbonatites. Mineral. Petrol. 98, 283–295.
Doroshkevich, A.G., Wall, F., Ripp, G.S., 2007a. Magmatic graphite in dolomite carbonatite at Pogranichnoe, North Transbaikalia, Russia. Contrib. Mineral. Petrol. 153, 339–353.
Doroshkevich, A.G., Wall, F., Ripp, G.S., 2007b. Calcite-bearing dolomite carbonatite dykes from Veseloe, North Transbaikalia, Russia and possible Cr-rich mantle xenoliths. Mineral. Petrol. 90, 19–49.
Egin, V.I., Kichigin, L.N., 1973. Characteristics and prospects of apatite mineralization in the Central Aldan. News of Yakutia Geology Vol. 3, pp. 75–80 (in Russian).
Entin, A.R., Tyan, O.A., 1984. Before-carbonatite Step of Formation of Apatite Deposits of Seligdar Type (Aldan). USSR SB RAS, Yakutsk (28 pp. (in Russian)).
Ernst, R.E., Bell, K., 2010. Large igneous provinces (LIPs) and carbonatites. Mineral. Petrol. 98, 55–76.
Ernst, R.E., Hamilton, M.A., Söderlund, U., Hanes, J.A., Gladkochub, D.P., Okrugin, A.V., Kolotilina, T., Mekhonoshin, A.S., Bleeker, W., LeCheminant, A.N., Buchan, K.L., Chamberlain, K.R., Didenko, A.N., 2016. Long-lived connection between southern Siberia and northern Laurentia in the Proterozoic. Nat. Geosci. 9, 464–469.
Fleck, R.J., Sutter, J.F., Elliot, D.H., 1977. Interpretation of discordant $^{40}Ar/^{39}Ar$ age-spectra of Mesozoic tholeiites from Antarctica. Geochim. Cosmochim. Acta 41 (1), 15–32.
Foley, S.F., Yaxley, G.M., Rosenthal, A., Buhre, S., Kiseeva, E.S., Rapp, R.P., Jacob, D.E., 2009. The composition of near-solidus melts of peridotite in the presence of CO_2 and H_2O between 40 and 60 kbar. Lithos 112S, 274–283.
Gladkochub, D.P., Donskaya, T.V., Ernst, R., Mazukabzov, A.M., Sklyarov, E.V., Pisarevsky, S.A., Wingate, M., Söderlund, U., 2012. Proterozoic basic magmatism of the Siberian craton: main stages and their geodynamic interpretation. Geotectonics 46 (4), 273–284.
Gladkochub, D.P., Pisarevsky, S.A., Donskaya, T.V., Natapov, L.M., Mazukabzov, A.M., Stanevich, A.M., Sklyarov, E.V., 2006. The Siberian craton and its evolution in terms of the Rodinia hypothesis. Episodes 29 (3), 169–174.
Günther, D., Heinrich, C.A., 1999. Enhanced sensitivity in laser ablation ICP-mass-spectrometry using helium-argon mixtures as aerosol carrier. J. Anal. At. Spectrom. 14, 1363–1368.
Günther, D., Audétat, A., Frischknecht, R., Heinrich, C.A., 1998. Quantitative analysis of major, minor and trace elements in fluid inclusions using laser ablation-inductively coupled plasma-mass spectrometry (LA-ICPMS). J. Anal. At. Spectrom. 13, 263–270.
Günther, D., Frischknecht, R., Heinrich, C.A., Kahlert, H.J., 1997. Capabilities of an argon fluoride 193 nm Excimer laser for laser ablation inductively coupled plasma mass

spectrometry microanalysis of geological materials. J. Anal. At. Spectrom. 12, 939–944.
Guo, Z.F., Hertogen, J., Liu, J.Q., Pasteels, P., Boven, A., Punzalan, L., He, H.Y., Luo, X.J., Zhang, W.H., 2005. Potassic magmatism in western Sichuan and Yunnan provinces, SE Tibet, China. J. Petrol. 46, 33–78.
Harlov, D.E., Förster, H.J., 2003. Fluid-induced nucleation of REE phosphate minerals in apatite: nature and experiment. Part II. Fluorapatite. Am. Mineral. 88, 1209–1229.
Harlov, D.E., Förster, H.J., Nijland, T.G., 2002. Fluid induced nucleation of REE-phosphate minerals in apatite: nature and experiment. Part I. Chlorapatite. Am. Mineral. 87, 245–261.
Harlov, D.E., Wirth, R., Förster, H.J., 2005. An experimental study of dissolution–reprecipitation in fluorapatite: fluid infiltration and the formation of monazite. Contrib. Mineral. Petrol. 150, 268–286.
Harmer, R.E., 1999. The petrogenetic association of carbonatite and alkaline magmatism: constraints from the Spitskop Complex, South Africa. J. Petrol. 40, 525–548.
Harmer, R.E., Gittins, J., 1998. The case for primary, mantle-derived carbonatite magma. J. Petrol. 39, 1895–1903.
Heinrich, C.A., Pettke, T., Halter, W.E., Aigner-Torres, M., Audétat, A., Günther, D., Hattendorf, B., Bleiner, D., Guillong, M., Horn, I., 2003. Quantitative multi-element analysis of minerals, fluid and melt inclusions by laser-ablation inductively-coupled-plasma mass-spectrometry. Geochim. Cosmochim. Acta 67, 3473–3497.
Hetherington, C.J., Harlov, D.E., 2008. Metasomatic thorite and uraninite inclusions in xenotime and monazite from granitic pegmatites, Hidra anorthosite massif, southwestern Norway: mechanics and fluid chemistry. Am. Mineral. 93, 806–820.
Hogarth, D.D., 1989. Pyrochlore, apatite and amphibole: distinctive minerals in carbonatite. In: Bell, K. (Ed.), Carbonatites: Genesis and Evolution, pp. 105–148.
Hou, Z., Tian, S., Yuan, Z., Xie, Y., Yin, S., Yi, L., Fei, H., Yang, Z., 2006. The Himalayan collision zone carbonatites in western Sichuan, SW China: petrogenesis, mantle source and tectonic implication. Earth Planet. Sci. Lett. 244, 234–250.
Klemme, S., van der Laan, S.R., Foley, S.F., Günther, D., 1995. Experimentally determined trace and minor element partitioning between clinopyroxene and carbonatite melt under upper mantle conditions. Earth Planet. Sci. Lett. 133, 439–448.
Larin, A.M., Kotov, A.B., Sal'nikova, E.B., Kovach, V.P., Makarev, L.B., Timashkov, A.N., Berezhnaya, N.G., Yakovleva, S.Z., 2000. New data on the age of granites of the Kodar and Tukuringra complexes, eastern Siberia: geodynamic constraints. Petrology 8 (3), 267–279.
Le Bas, M.J., 2008. Fenites associated with carbonatites. Can. Mineral. 46, 915–932.
Lee, W., Wyllie, P.J., 1998. Petrogenesis of carbonatite magmas from mantle to crust, constrained by the system CaO-(MgO + FeO*)-(Na_2O + K_2O)-(SiO_2 + Al_2O_3 + TiO_2)-CO_2. J. Petrol. 39, 495–517.
Li, H., Zhou, M.F., 2015. Multiple stages of hydrothermal REE remobilization recorded in fluorapatite in the Paleoproterozoic Yinachang Fe–Cu–(REE) deposit, Southwest China. Geochim. Cosmochim. Acta 166, 53–73.
Longerich, H.P., Jackson, S.E., Günther, D., 1996. Laser ablation inductively coupled plasma mass spectrometric transient signal data acquisition and analyte concentration calculation. J. Anal. At. Spectrom. 11 (9), 899–904.
Ludwig, K.R., 1999. Isoplot/Ex. Version 2.10. User's Manual. Berkeley Geochronology Center Special Publication Vol. 1 (46 pp.).
Ludwig, K.R., 2000. SQUID 1.00. User's Manual. Berkeley Geochronology Center Special Publication Vol. 2 (19 pp.).
Mekhonoshin, A.S., Ernst, R., Soderlund, U., Hamilton, M.A., Kolotilin, A.T.B., Izokh, A.E., Polyakov, G.V., Tolstykh, N.D., 2016. Relationship between platinum-bearing ultramafic-mafic intrusions and large igneous provinces (exemplified by the Siberian craton). Russ. Geol. Geophys. 57 (5), 822–833.
Minin, V.A., Vasilenko, V.B., Kuznetsova, L.G., Prugov, V.P., 2016. To mineralogy of calcite-magnetite-apatite-serpentine rocks of the Seligdar deposit (Yakutia). Zapiski RMO CXLV (1), 80–104.
Neimark, L.A., Larin, A.M., Nemchin, A.A., Ovchinnikova, G.V., Rytsk, E.Y., 1998. Geochemical, geochronological (U–Pb) and isotopic (Pb, Nd) evidence of anorogenic magmatism in the North Baikal volcanoplutonic belt. Petrology 6 (4), 139–164.
Nozhkin, A.D., Bibikova, E.V., Turkina, O.M., Ponomarchuk, V.A., 2003. U–Pb, Ar–Ar, and Sm–Nd isotope-geochronological study of porphyritic subalkalic granites of the Taraka pluton (Yenisei Range). Russ. Geol. Geophys. 44 (9), 879–889 (842–852).
Osorgin, N.Y., 1990. Chromatographic Analysis of the Gas Phase in Minerals (Methods, Equipment, Metrology) (Novosibirsk: Preprint N11: 32 (in Russian)).
Otto, J.W., Wyllie, P.J., 1993. Relationship between silicate melts and carbonate precipitating melts in CaO–MgO–SiO_2–CO_2–H_2O at 2 kbar. Mineral. Petrol. 48, 343–365.
Parsons, I., Brown, W.L., 1988. Sidewall crystallization in the Klokken intrusion: zoned ternary feldspars and coexisting minerals. Contrib. Mineral. Petrol. 98, 431–444.
Pirajno, F., González-Álvarez, I., Chen, W., Simonetti, A., Kyser, K., leGrass, M., 2014. The Gifford Creek ferrocarbonatite complex, Gascoyne Province, Western Australia: associated fenitic alteration and a putative link with the ~1075 Ma Warakurna LIP. Lithos 202–203, 100–119.
Popov, N.V., Kotov, A.B., Postnikov, A.A., Sal'nikova, E.B., Shaporina, M.N., Larin, A.M., Yakovleva, S.Z., Plotkina, Y.V., Fedoseenko, A.M., 2009. Age and tectonic position of the Chiney Layered Massif, Aldan shield. Dokl. Earth Sci. 424 (1), 64–67.
Prokopyev, I.R., Borisenko, A.S., Borovikov, A.A., Pavlova, G.G., 2016. Origin of REE-rich ferrocarbonatites in southern Siberia (Russia): implications based on melt and fluid inclusions. J. Mineral. Petrol. http://dx.doi.org/10.1007/s00710-016-0449-z (available online).
Prokopyev, I.R., Borovikov, A.A., Pavlova, G.G., Borisenko, A.S., 2014. The role of chloride-carbonate melts in the formation of sideritic carbonatites of the Karasug Fe-F-REE deposit (Tyva Republic, Russia). Dokl. Earth Sci. 455, 446–449.
Puzanov, L.S., Partsevsky, A.I., 1978. About genetic type of the Seligdar apatite deposit (Central Aldan). Doklady USSR RAS Vol. 243 (1), pp. 163–179 (in Russian).
Shokhonova, M.N., Donskaya, T.V., Gladkochub, D.P., Mazukabzov, A.M., Paderin, I.P., 2010. Paleoproterozoic basaltoids in the North Baikal volcanoplutonic belt of the Siberian craton: age and petrogenesis. Russ. Geol. Geophys. 51, 815–832.
Smirnov, F.L., Marshintsev, Z.K., Moskvitina, A.V., et al., 1976. Typomorphic features of apatite deposits and occurrences of the Aldan Shield. Phosphorus Geochemistry and Mineralogy Characteristics of Apatite. Yakutsk, USSR SB RAS, pp. 5–31 (in Russian).
Sweeney, R.J., 1994. Carbonatite melt compositions in the Earth's mantle. Earth Planet. Sci. Lett. 128, 259–270.
Sweeney, R.J., Prozesky, V., Przybylowicz, W., 1995. Selected trace and minor element partitioning between peridotite minerals and carbonatite melts at 18–46 kbar pressure. Geochim. Cosmochim. Acta 59, 3671–3683.
Tolstykh, N.D., Orsoev, D.A., Krivenko, A.P., Izoch, A.E., 2008. Noble Metals in Layered Ultrabasic-basic Massifs in the Southern Part of Siberian Platform. Parallel (Novosibirsk, 194 pp.).
Travin, A.V., Yudin, D.S., Vladimirov, A.G., Khromykh, S.V., Volkova, N.I., Mekhonoshin, A.S., Kolotilina, T.B., 2009. Thermochronology of the Chernorudsky granulite zone (Ol'khon region, western Cisbaikalia). Geochem. Int. 11, 1181–1199.
Tropper, P., Manning, C.E., Harlov, D.E., 2011. Solubility of $CePO_4$ monazite and YPO_4 xenotime in H_2O and H_2O–NaCl at 800 °C and 1 GPa: implications for REE and Y transport during high-grade metamorphism. Chem. Geol. 282, 58–66.
Tropper, P., Manning, C.E., Harlov, D.E., 2013. Experimental determination of $CePO_4$ and YPO_4 solubilities in H_2O–NaF at 800 °C and 1 GPa: implications for rare earth element transport in high-grade metamorphic fluids. Geofluids 13, 372–380.
Tugarinov, A.I., Bibikova, E.V., Gracheva, T.V., Lyalikov, A.V., 1976. The problem of an age for Iengrskoy series in Aldan shield. Dokl. Akad. Nauk USSR 231 (1), 169–172 (in Russian).
Turkina, O.M., Bibikova, E.V., Nozhkin, A.D., 2003. Stages and geodynamic settings of Early Proterozoic granite formation on the southwestern margin of the Siberian craton. Dokl. Earth Sci. 389 (2), 159–163.
Ulrich, T., Günther, D., Heinrich, C.A., 2001. The evolution of a porphyry Cu-Au deposit, based on LA-ICP-MS analysis of fluid inclusions: Bajo de la Alumbrera, Argentina. Econ. Geol. 96, 1743–1774.
Vasilenko, V.B., Kuznetsova, L.G., Kholodova, L.D., et al., 1982. Apatite Rocks of the Seligdar. Nauka, Novosibirsk (213 pp. (in Russian)).
Vrublevskii, V.V., Pokrovskii, B.G., Zhuravlev, D.Z., Anoshin, G.N., 2003. Composition and age of pechenga linear carbonatite complex, Eniseyskii kryazh. Petrology 11, 130–147.
Williams, J.S., 1998. U-Th-Pb geochronology by ion microprobe. Application of microanalytical techniques to understanding mineralizing processes. Rev. Econ. Geol. 7, 1–35.
Williams-Jones, A.E., Migdisov, A.A., Samson, I.M., 2012. Hydrothermal mobilization of the rare earth elements-a tale of "Ceria" and "Yttria". Elements 8, 355–360.